Journal of Nanophotonics

Nanophotonics.SPIEDigitalLibrary.org

Integrated photonic crystal selective emitter for thermophotovoltaics

Zhiguang Zhou
Omar Yehia
Peter Bermel

SPIE.

Integrated photonic crystal selective emitter for thermophotovoltaics

Zhiguang Zhou,[a] Omar Yehia,[b] and Peter Bermel[a,*]

[a]Purdue University, School of Electrical and Computer Engineering and Birck Nanotechnology Center, 1205 West State Street, West Lafayette, Indiana 47907, United States

[b]Purdue University, School of Mechanical Engineering, 585 Purdue Mall, West Lafayette, Indiana 47907, United States

Abstract. Converting blackbody thermal radiation to electricity via thermophotovoltaics (TPV) is inherently inefficient. Photon recycling using cold-side filters offers potentially improved performance but requires extremely close spacing between the thermal emitter and the receiver, namely a high view factor. Here, we propose an alternative approach for thermal energy conversion, the use of an integrated photonic crystal selective emitter (IPSE), which combines two-dimensional photonic crystal selective emitters and filters into a single device. Finite difference time domain and current transport simulations show that IPSEs can significantly suppress sub-bandgap photons. This increases heat-to-electricity conversion for photonic crystal based emitters from 35.2 up to 41.8% at 1573 K for a GaSb photovoltaic (PV) diode with matched bandgaps of 0.7 eV. The physical basis of this enhancement is a shift from a perturbative to a nonperturbative regime, which maximized photon recycling. Furthermore, combining IPSEs with nonconductive optical waveguides eliminates a key difficulty associated with TPV: the need for precise alignment between the hot selective emitter and cool PV diode. The physical effects of both the IPSE and waveguide can be quantified in terms of an extension of the concept of an effective view factor. [DOI: 10.1117/1.JNP.10.016014]

Keywords: integrated photonic crystal; selective emitter; thermophotovoltaics; effective view factor; waveguide.

Paper 15111P received Sep. 24, 2015; accepted for publication Feb. 11, 2016; published online Mar. 8, 2016.

1 Introduction

Thermophotovoltaics (TPV) convert heat to electricity via thermal radiation. Photons with energies below the bandgap of the photovoltaic (PV) diode, resulting from the broad spectrum of the Planck blackbody distribution, are generally the dominant source of loss in TPV systems. Fortunately, these energy losses can be eliminated by selective emitters that have near-blackbody emission above the PV bandgap and low emission below the PV bandgap.[1] Several materials have been proposed for selective emission, including plasmonic metamaterials,[2–4] refractory plasmonic structures,[5] rare earth materials,[6–8] and photonic crystals (PhCs).[9–24] However, realistic selective emitters still have residual low energy emission near the bandgap that can considerably limit the conversion efficiency. Significant improvement can be achieved by the use of cold-side PhC filters, including plasma filters, quarter-wave stacks,[25] and rugate filters.[26] These filters essentially reflect the low-energy photons back to the selective emitter, in a process known as photon recycling.[27–32] In order to achieve sufficient photon recycling, proximity between the emitter and filter is required.[33] In the typical cold-side filter configurations, where the filter is attached to the PV diode as an entire receiver, this requirement can be quantified by the view factor from the emitter to the receiver, which is the probability that emitted photons reach the receiver. Certain strategies, such as micro-gap or nanoscale-gap TPV, in fact require extremely

*Address all correspondence to: Peter Bermel, E-mail: pbermel@purdue.edu

high view factors to achieve evanescent coupling.[34–36] However, it is extremely difficult to achieve high view factors in experiments, since a constant gap d must be maintained between two surfaces when the distance is orders of magnitude smaller than the lateral width w of each surface. The angular tolerance $\theta_{\mathrm{tol}} = \tan^{-1}(d/w)$ is impractically low. Although ultranarrow (scanning electron microscope-like) tips can achieve such small gaps, the associated power produced is extremely small.

Despite the great potential for the improvement of TPV associated with these various approaches, certain common challenges remain in translating these ideas into experiment. One major difficulty is in achieving and maintaining sufficiently selective thermal emission. While simpler structures can be fabricated with high fidelity, their selectivity is often lacking, while more complex monolithic structures with higher potential selectivity are more vulnerable to fabrication error and degradation, which becomes even more severe with finer features.[37] Composite structures consisting of simple emitters and cold-side PhC reflectors also have potential for highly selective effective emissivity, but these give rise to a second common problem: achieving precise alignment between a hot emitter and cold receiver. Unfortunately, configurations requiring the greatest precision are the same as those with the highest power generation potential. In order to overcome this challenge, it is important to fundamentally reexamine the geometric configuration of the three key objects: emitter, filter, and PV diode. While it is exceedingly difficult to bring the PV diode in contact with the emitter, it is certainly conceivable to bring the emitter and filter together. However, it is quite likely that a filter made exclusively of insulating materials would be a poor conductor of heat and thus would experience a significant thermal gradient. Therefore, a different treatment is needed, which correctly accounts for both the thermal gradient and potential for incoherent radiative exchange between the emitter and filter in proximity.

Thus, in this work, we propose an alternative approach for high-performance TPV systems capable of simultaneously addressing problems with long-lasting selectivity and alignment, known as an integrated photonic crystal selective emitter (IPSE), and develop a corresponding framework to analyze its performance. The IPSE combines the PhC selective emitter and the filter as an integrated whole, such that the view factor from the emitter to the filter approaches unity and is independent of the view factor from the emitter to the receiver (PV diode). This approach also sidesteps the difficulties of the nanoscale-gap regime, since no gap is required. Photon recycling and reabsorbed power can therefore no longer be considered as a perturbation;[33] instead, new physical effects should arise in this nonperturbative regime. Finite difference time-domain (FDTD)[38] and current transport simulations have shown that an IPSE enables system conversion efficiencies to reach up to 41.8%, using the realistic model for GaSb PV diodes, by nearly eliminating sub-bandgap emission. This corresponds to showing that the 10.9% gap from the ideal efficiency value observed in previous work[39] can now be reduced to 4.3% using IPSEs. Arguably, the IPSE creates a nonzero chemical potential for photon emission using a purely thermal input source, which is a fundamentally distinctive physical behavior akin to light-emitting diodes.[40] Further, the IPSE is relatively amenable to fabrication in the near term, with key features already achieved in previous experimental work.[20–22,25,26]

2 Design of the Integrated Photonic Crystal Selective Emitter

As shown in Fig. 1(a), the IPSE consists of a metal two-dimensional (2-D) PhC and a chirped quarter-wave stack (QWS), which are brought to an extremely small separation. The metal 2-D PhC consists of an array of holes filled entirely with low refractive index material, so that the bilayer structure can be fabricated and firmly attached to the emitter without greatly increasing sub-bandgap emission.[41,42] The chirped QWS structure placed directly atop the PhC consists of two alternating dielectric materials with different refractive indices. In such an integrated design, where the view factor approaches unity, all thermal photons emitted from the front surface of the 2-D PhC would be filtered. For the highest possible performance, it is essential to have either a backreflector or another PV diode on the opposite side.

In this work, the IPSE is examined directly as a whole using a TPV simulation tool developed by the present authors.[43,44] The emittance spectrum associated with the design is first calculated

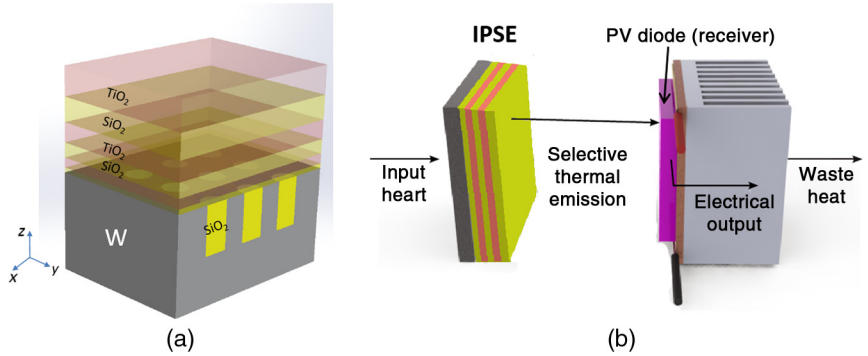

Fig. 1 Design of the IPSE. (a) Cutaway view of the IPSE, made of a chirped one-dimensional PhC filter, consisting of low-index SiO_2 and high-index TiO_2, integrated with a 2-D tungsten PhC structure filled with SiO_2. (b) Schematic depicting a high-performance TPV system utilizing an IPSE.

using an FDTD simulation method known as MIT electromagnetic equation propagation.[45] Then the current–voltage $(J-V)$ relation for TPV cells is calculated from the emittance spectrum assuming zero series resistance, as in previous work.[33] The effect of finite series resistance is considered later in this work. The power output is then calculated by solving for the maximum power point via $d(JV)/dV = 0$. Based on the experimental performance of metalorganic vapor phase epitaxial grown low-bandgap III-V PV diodes from Lincoln Laboratories, an average external quantum efficiency of 82% is assumed.[33] The thermal power input is calculated as the total thermal emission less the power reabsorbed by the emitter. The system conversion efficiency η is then finally given as

$$\eta = \frac{I_{\mathrm{sc}} V_{\mathrm{oc}} \mathrm{FF}}{P_{\mathrm{em}} - P_{\mathrm{re}}}. \tag{1}$$

The geometry of the 2-D PhC emitter follows from our recent work on the performance of tungsten (W) PhC selective emitters.[39] Previously, we found that for a W PhC emitter paired with a cold-side rugate filter,[46] the highest estimated $\eta = 35.2\%$ occurs at $E_g = 0.7$ eV and $T = 1573$ K, where E_g is the bandgap energy of the PV diode and T is the operating temperature of the emitter. A suitable geometry for selective emission is determined using the technique of quality factor-matching, in which the radiative coupling rate is matched with the material absorption rate to achieve full absorption. In this proposed structure, the array of holes is filled with SiO_2; therefore, the optimal 2-D hole array geometry needs to be rescaled by the refractive index $n_{\mathrm{SiO_2}} = 1.46$, giving $r = 0.2604$ μm, $d = 2.1172$ μm, and $a_x = a_y = 0.6356$ μm. Here, r is the hole radius, d is the hole depth, and a_x and a_y are the periods of the array along the x and y directions. Maxwell's equations make these photonic structures completely scalable in principle.[10] The key constraint is to find a pair of materials with sufficient refractive index values and very low losses; this criterion generally excludes frequencies in ultraviolet or above.

It will now be shown that IPSEs can lead to performance improvements over bare W PhCs, which help approach the limits of an ideal selective emitter. For specificity, we consider the case of a bandgap $E_g = 0.7$ eV. The ideal selective emitter for such a bandgap has a top hat emittance spectrum depicted by the red curves in Fig. 2, corresponding to 100% emittance between 1300 and 1771 nm, and zero emittance elsewhere. This property fully suppresses sub-bandgap losses and greatly reduces carrier thermalization,[47] yielding an ideal emission conversion efficiency $\eta_{\mathrm{ideal}} = 46.1\%$.

2.1 *Integrated Photonic Crystal Selective Emitter with Chirped Quarter-Wave Stack*

Now we consider the efficiency of an appropriate IPSE structure for comparison. The integrated SiO_2/TiO_2 ($n_{\mathrm{TiO_2}} = 2.50$) QWS has a cutoff wavelength at 1771 nm, matching the PV bandgap energy of 0.7 eV. The bilayer structure has an initial bilayer thickness of 497 nm, which is

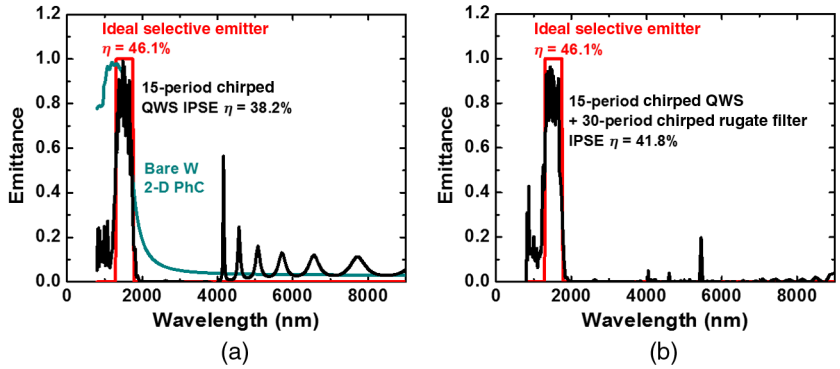

Fig. 2 Emittance spectrum comparisons. (a) Emittance spectrum of 15-period QWS IPSE (black) in comparison to the emittance spectrum of an ideal emitter (red) and a bare W photonic crystal emitter (blue). Parasitic emission from 1771 to 4000 nm is effectively suppressed, but strong parasitic emission occurs beyond 4000 nm. (b) Emittance spectrum of 15-period QWS + 30-period rugate filter IPSE (black) in comparison to the emittance spectrum of an ideal emitter (red).

chirped linearly upward at a rate of 5.1% per bilayer to make a broadband filter. It is important to limit the chirping rate and material choices here to suppress the emergence of anomalies in the photonic density of states (analogous to a Wannier-Stark ladder in electronic structures). At the selected chirping rate, the emittance spectrum of a 15-period QWS IPSE is simulated and displayed as a black curve in Fig. 2(a). At $T = 1573$ K, the spectrally averaged effective emittance from 1771 to 9000 nm is $\varepsilon_{\text{eff}} = 0.02$; for useful emission, it is $\varepsilon_{\text{eff}} = 0.71$. These calculations assume that the material parameters are unchanged from literature values at the targeted temperature.[48] Compared to the bare W PhC (without an integrated filter) results, shown as the blue curve in Fig. 2(a), it is immediately obvious that the IPSE strongly suppresses parasitic emittance from the cutoff wavelength of 1771 up to 4000 nm, but strong parasitic emission occurs between 4000 and 9000 nm, as shown in Fig. 2(a). The conversion efficiency η calculated using the emittance spectrum up to 9000 nm is 38.2%. Thus, an increase in η of 3% is achieved at 1573 K, since the major parasitic emission is beyond the blackbody peak.

The performance of the 15-period QWS IPSE here is still 7.89% below the ideal case. The reason for this difference can be analyzed by comparing with the ideal emitter and quantifying the loss mechanism. Three sources of efficiency losses are considered in Table 1: (1) emission at wavelengths shorter than 1300 nm, (2) imperfect emission between 1300 and 1771 nm, and (3) parasitic emission at wavelengths from 1771 to 9000 nm. Wavelengths beyond 9000 nm are emitted even at room temperature; the power is small enough in this region to be neglected. Even if we assume a constant emittance of 0.1 from 9000 up to 15,000 nm, the efficiency loss at 1573 K is <0.1%. The primary nonideality comes from parasitic emission, particularly between 4000 and 9000 nm, which contributes a 4% efficiency loss. Therefore, further suppression of the parasitic emission is required. However, increasing the number of bilayers or the chirping rate will shift the high-order reflections to longer wavelengths, suppressing useful emission between 1300 and 1771 nm, and thus is not a viable option.

Table 1 Classification of physical loss mechanisms affecting TPV efficiency η. By modifying the structure of the IPSE, parasitic emission is reduced while useful emission is enhanced, allowing efficiencies to more closely approach the ideal value of 46.1%.

IPSE structure	Conversion efficiency η (%)	Total losses in efficiency (%)	Short-wavelength emission (%)	Insufficient emission (%)	Parasitic emission (%)
15-period QWS IPSE	38.2	7.89	0.80	1.71	5.38
15-period QWS + 30-period rugate filter IPSE	41.8	4.29	0.89	1.66	1.74

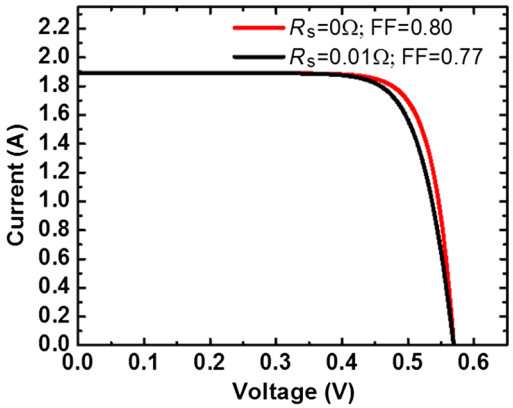

Fig. 3 Calculated light $I-V$ curve for the experimentally based GaSb PV diode, when illuminated by the 15-period QWS + 30-period rugate filter IPSE at 1573 K. Two cases are shown: series resistance $R_s = 0\ \Omega$ (red) and $R_s = 0.01\ \Omega$ (black).

2.2 *Integrated Photonic Crystal Selective Emitter with Chirped Quarter-Wave Stack and Chirped Rugate Filter*

In order to suppress parasitic emission while preserving useful emission, we instead introduce a chirped 30-period rugate filter on top of the 15-bilayer IPSE structure. Rugate filters use a different refractive index profile, more akin to a sinusoid, which eliminates higher-order reflections.[26] In this case, our rugate filter is composed of six different materials, with varying indices of refraction from $n_{SiO_2} = 1.46$ to $n_{TiO_2} = 2.50$. Each layer thickness is determined by following the type C design from Carniglia,[46] with the cutoff wavelength designed at 3500 nm and a linear chirping rate of 3.5%. The simulated emittance spectrum in Fig. 2(b) shows that the rugate filter provides effective suppression of parasitic emission from 4000 to 9000 nm. The effective emittance of parasitic emission from 1771 to 9000 nm is greatly reduced to $\varepsilon_{\text{eff}} = 0.004$, while that of useful emission actually increases to $\varepsilon_{\text{eff}} = 0.74$, using the same assumptions as before. Overall conversion efficiency η is thus increased to 41.8%. Similar analysis of loss mechanism for the IPSE with 30-period rugate filter on top is summarized in Table 1. The efficiency loss due to the first two categories is close to the 15-bilayer IPSE structure, showing that the emission at wavelengths shorter than 1771 nm is preserved by the pass-band of the rugate filter. The parasitic loss is significantly reduced by the broader stop-band of the rugate filter. Overall, the efficiency gap from the ideal case is substantially reduced to 4.3%, which is less than two-fifths of the original gap previously seen in the literature.[39]

Assuming the presence of a large-area passive heat sink with convective and radiative cooling available on its outer surface, the best IPSE design leaves the temperature of the PV diode at 1.5 K above ambient when illuminated. It was also assumed that the PV diode has zero series resistance. Here, we consider the impact of a finite series resistance on the system conversion efficiency. A typical GaSb PV diode produced by JX Crystals has a series resistance $R_s = 0.01\ \Omega$ (the value is fitted from the experimental $I-V$ curve under illumination of a 1200°C emitter provided by JX Crystals). The light $I-V$ curve of GaSb PV diode illuminated by the 15-period QWS + 30-period rugate filter IPSE at 1573 K is calculated with $R_s = 0.01\ \Omega$, as seen by the black curve in Fig. 3. Compared to the case where zero R_s is assumed, the fill factor decreases from 80 to 77% when $R_s = 0.01\ \Omega$, reducing the conversion efficiency to $\eta = 40.3\%$.

3 Perturbative and Nonperturbative Photon Recycling

Next, the new physical effects that arise in TPV systems that use IPSEs are examined from the aspect of radiation heat transfer. Generally, the differential view factor for the n'th reflection between the emitter and the receiver can be defined as follows:

$$dF_n = \frac{\cos^2\theta_n}{\pi d_n^2} dA_{n+2}, \tag{2}$$

where dF_n is the differential view factor for the n'th reflection; d_n is the distance from the original emitter A_1 to the n'th reflection image surface A_{n+2};[49] θ_n is the angle between the surface normal of the differential area dA_1 and the line connecting two differential areas dA_1 and dA_{n+2}. The integrated view factor F_n can be calculated as shown in Ref. 50.

The n'th contribution to the short-circuit current for a given wavelength λ is then calculated by

$$I_{sc}(\lambda) = \sum_{n=0,2\ldots}^{\infty} A_1 \frac{2qc\mathrm{EQE}(\lambda)(R_1R_2)^{n/2}\varepsilon(\lambda)}{\lambda^4\left[\exp\left(\frac{hc}{\lambda kT}\right)-1\right]} F_n = \sum_{n=0,2\ldots}^{\infty} B_n(\lambda)F_n, \tag{3}$$

where F_n is the n'th-order view factor and B_n is the coefficient corresponding to the n'th reflection; $\mathrm{EQE}(\lambda)$ is the external quantum efficiency of the PV diode; R_1 and R_2 are the reflectivities of the emitter and receiver, respectively; h is the Planck's constant; k is the Boltzmann's constant; c is the speed of light. Since R_2 is very small for photons above the bandgap, $I_{sc}(\lambda)$ is approximated as $I_{sc}(\lambda) \approx B_0F_0$.

When a cold-side filter is applied, photon recycling in the TPV system is expressed using a power series (in the perturbative regime). The recycled power at a given wavelength λ can be calculated as

$$P_{re}(\lambda) = \sum_{n=1,3\ldots}^{\infty} A_1 I_{BB}(\lambda) R_2^{(n+1)/2} R_1^{(n-1)/2}(1-R_1)\varepsilon(\lambda)F_n = \sum_{n=1,3\ldots}^{\infty} C_n(\lambda)F_n, \tag{4}$$

where $I_{BB}(\lambda)$ is the blackbody radiation power density at wavelength λ and C_n is the coefficient corresponding to the n'th reflection. Specifically, for TPV systems using selective emitters and nonideal filters, $P_{re}(\lambda)$ can be approximated as $P_{re}(\lambda) \approx C_1F_1$. Substituting I_{sc} and P_{re} in Eq. (1) with Eqs. (3) and (4), the TPV conversion efficiency, including photon recycling, can be calculated as

$$\eta = \frac{BV_{oc}\mathrm{FF}}{P_{em}(1-\kappa)} F_{eff}, \tag{5}$$

$$F_{eff} \equiv \frac{F_0(1-\kappa)}{1-\kappa F_1}, \tag{6}$$

where $B = \int B_0(\lambda)\mathrm{d}\lambda$; $C = \int C_1(\lambda)\mathrm{d}\lambda$; F_{eff} is defined as the effective view factor, whose physical meaning is the ratio between the useful photons received by the receiver and the total emitted photons excluding the reabsorbed ones; $\kappa \equiv C/P_{em}$ is the ratio between the maximum recycled power and the initial emitted power P_{em}; V_{oc} is the open-circuit voltage. Since the effective view factor is not linearly dependent on the actual view factor F_0, a nonlinear dependence of η on the view factor is expected in the perturbative regime.

However, in the nonperturbative regime, the view factor from the emitter to the filter approaches unity, while the view factor from the IPSE to the PV diode is still F_0. The reabsorbed power P_{re} is now a constant instead of a function of F_1 (or F_0). Thus, $F_{eff} = F_0$, so Eq. (5) should be modified as

$$\eta = \frac{B'V_{oc}\mathrm{FF}}{P_{em}(1-\kappa)} F_0, \tag{7}$$

where $B' = \int B_0'(\lambda)\mathrm{d}\lambda$; $B_0'(\lambda)$ is similarly defined by Eq. (3) but using different parameters. Since the photon recycling perturbation is eliminated, linear view factor dependence is thus expected in the nonperturbative regime.

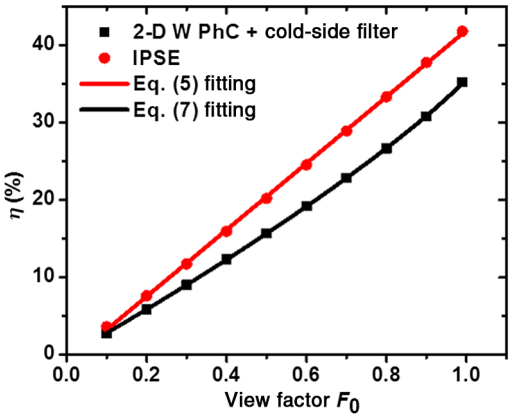

Fig. 4 Conversion efficiency η as a function of view factor F_0 for a TPV system using a 15-period QWS + 30-period rugate filter IPSE and a TPV system using a cold-side rugate filter. The distinctive behaviors of the perturbative and nonperturbative regimes are successfully described by Eqs. (5) and (7), which incorporate the analytically calculated effective view factor.

The system conversion efficiency of a TPV system using IPSE is now simulated at different view factors (with respect to the receiver), using a TPV simulation tool developed by the authors. For comparison, the same approach is also employed to simulate a TPV system with a cold-side rugate filter attached to the PV diode (in the perturbative regime). Equations (5) and (7) are then used to fit the results of the perturbative and the nonperturbative cases respectively, as shown in Fig. 4. The fits are in perfect agreement with the simulation results in each case. The linear view factor dependence of a TPV system where IPSE is applied shows that the photon recycling is no longer influenced by the spacing between the emitter and the receiver. Thus, an extremely high view factor for sufficient photon recycling is no longer necessary. The distinction between the behavior in the perturbative and nonperturbative regimes is very accurately described by Eqs. (5) and (7). Therefore, F_{eff} correctly captures the physics of photon recycling in TPV systems and can be used as a metric to describe most TPV systems (both in the perturbative and nonperturbative regimes).

4 Thermophotovoltaics System with Photonic Crystal Waveguide

Furthermore, F_{eff} can be increased much further by surrounding the gap between the emitter and the receiver with a waveguide as shown in Fig. 5(a). The requirements for high reflectivity at specific wavelengths and low thermal conductivity could be satisfied by the use of dielectric PhC waveguides. To include the impact of the waveguide on the TPV systems, the expressions for F_0 and F_1 can be generalized as

$$F_0^{\text{wg}} \approx F_0 + (1 - F_0)\frac{f^2 R\gamma}{1 - Rf(1-\gamma)}, \tag{8}$$

$$F_1^{\text{wg}} \approx F_1 + (F_0^{\text{wg}} - F_1)\frac{f^2 R\gamma}{1 - Rf(1-\gamma)}, \tag{9}$$

where f represents both the view factor from the emitter to the waveguide and from the waveguide to the receiver, respectively; R is the reflectivity of the sidewalls of the waveguide; γ is the area ratio between the emitter and the waveguide; all the view factors with the superscript wg capture the effect of waveguiding. Figures 5(b) and 5(c) show the contour plots of both F_0^{wg} and F_1^{wg} as functions of the original view factor F_0 and the reflectivity R of waveguide, assuming that the waveguide is in proximity to both the emitter and the receiver ($f = 0.99$) and the cross-section of the waveguide is the same as the surface area of the emitter. Significant improvement in F_0^{wg} and F_1^{wg} can be achieved when a highly reflective waveguide is applied. Especially when

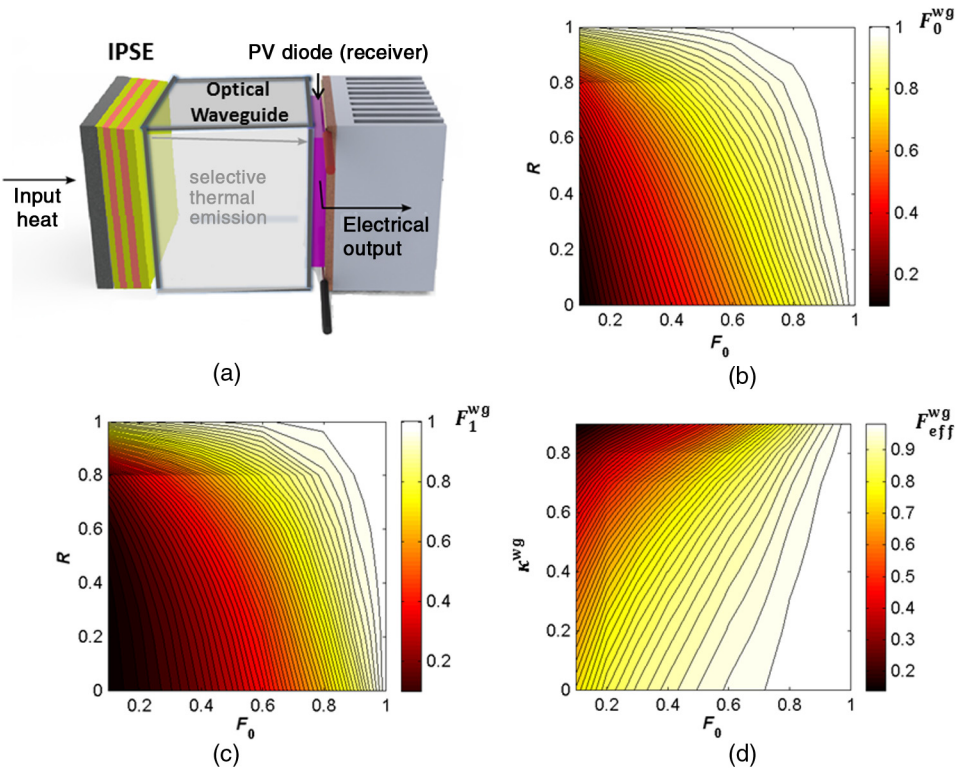

Fig. 5 Waveguide and contour plots. (a) A TPV IPSE surrounded by a dielectric waveguide reduces the need for close alignment between emitter and receiver for improved efficiency. (b) Contour plot of F_0^{wg} as a function of original view factor F_0 and reflectivity R of the waveguide. (c) Contour plot of F_1^{wg} as a function of original view factor F_0 and reflectivity R of the waveguide. (d) Contour plot of F_{eff}^{wg} as a function of original view factor F_0 and maximum recycled power ratio κ^{wg} contributed only by the waveguide.

waveguides with $R \approx 0.99$ is added, both F_0^{wg} and F_1^{wg} will be close to unity even with an original view factor as low as 0.28, a view factor corresponding to a length of waveguide enough to make the thermal power conduction less than 0.1% of the overall heat transfer. From Eqs. (3) and (4), it can be predicted that both the short-circuit current and the reabsorbed power will be considerably improved if a highly reflective waveguide is used. The effective view factor F_{eff}^{wg} including the waveguide can be calculated as

$$F_{eff}^{wg} \equiv \frac{F_0^{wg}(1-\kappa^{wg})}{1-\kappa^{wg}F_1^{wg}}, \tag{10}$$

where κ^{wg} is the ratio between the maximum recycled power contributed by the waveguide only to the initial emitted power P_{em}. Figure 5(d) shows the contour plot of F_{eff}^{wg} as a function of κ^{wg} and the original view factor F_0, assuming a realistic waveguide with $R = 0.95$ is added. The IPSE almost eliminates the need for photon recycling between the emitter and the PV diode. Therefore, κ^{wg} in this case is close to zero, giving an F_{eff}^{wg} close to 0.9, even with $F_0 = 0.28$. It is obvious that using a waveguide can greatly improve F_{eff}, which could be extremely useful for maintaining physical separation between a hot emitter and cold PV diode.

5 Conclusion

In conclusion, the IPSE and waveguide eliminate losses, due to the nonideal photon recycling between the emitter and the receiver, as well as the difficulty of close alignment between a hot emitter and cold receiver. This approach can increase the theoretical conversion efficiency of a TPV system from the prior value of 35.2% up to 41.8% at 1573 K. Such behavior is described by

analytical expressions based on our extended definition of the effective view factor F_{eff}. Our approach captures the physics of TPV systems where Kirchoff's law cannot be applied directly, particularly in the presence of photon recycling and waveguides. It is also consistent with previous results in the field.[20,41,42] This extended definition of effective view factor can be broadly applied to any TPV system, and could even lead to further improvements in system conversion efficiencies and experimental fabrication, through the use of dielectric PhC waveguides.

Acknowledgments

We thank Qingshuang Chen for providing access to simulation capabilities for this study, as well as Enas Sakr and Chao Zhou for valuable discussions. Support was provided by the Department of Energy, under DOE Cooperative Agreement No. DE-EE0004946 (PVMI Bay Area PV Consortium), the Semiconductor Research Corporation, under Research Task No. 2110.006 (Network for Photovoltaic Technologies), and the National Science Foundation, under Award EEC1454315-CAREER: Thermophotonics for Efficient Harvesting of Waste Heat as Electricity. Computational resources on nanoHUB.org were provided by the Network for Computational Nanotechnology, which is funded by the U.S. National Science Foundation under Grant No. EEC-1227110.

References

1. T. Bauer, *Thermophotovoltaics: Basic Principles and Critical Aspects of System Design*, Springer Science & Business Media, Heidelberg, Germany (2011).
2. S. A. Maier, *Plasmonics: Fundamentals and Applications*, Springer Science & Business Media, New York (2007).
3. W. Cai and V. M. Shalaev, *Optical Metamaterials*, Springer, New York (2010).
4. C. Wu et al., "Metamaterial-based integrated plasmonic absorber/emitter for solar thermophotovoltaic systems," *J. Opt.* **14**, 024005 (2012).
5. U. Guler, A. Boltasseva, and V. M. Shalaev, "Refractory plasmonics," *Science* **344**, 263–264 (2014).
6. B. Bitnar et al., "Characterisation of rare earth selective emitters for thermophotovoltaic applications," *Sol. Energy Mater. Sol. Cells* **73**, 221–234 (2002).
7. D. L. Chubb et al., "Rare earth doped high temperature ceramic selective emitters," *J. Eur. Ceram. Soc.* **19**, 2551–2562 (1999).
8. E. S. Sakr, Z. Zhou, and P. Bermel, "High efficiency rare-earth emitter for thermophotovoltaic applications," *Appl. Phys. Lett.* **105**, 111107 (2014).
9. P. Bermel et al., "Design and global optimization of high-efficiency thermophotovoltaic systems," *Opt. Express* **18**(Suppl 3), A314–A334 (2010).
10. J. D. Joannopoulos et al., *Photonic Crystals: Molding the Flow of Light*, Princeton University Press, Princeton (2011).
11. H. Sai, Y. Kanamori, and H. Yugami, "High-temperature resistive surface grating for spectral control of thermal radiation," *Appl. Phys. Lett.* **82**, 1685–1687 (2003).
12. H. Sai and H. Yugami, "Thermophotovoltaic generation with selective radiators based on tungsten surface gratings," *Appl. Phys. Lett.* **85**, 3399–3401 (2004).
13. I. Celanovic, D. Perreault, and J. Kassakian, "Resonant-cavity enhanced thermal emission," *Phys. Rev. B* **72**(7), 2–7 (2005).
14. D. L. C. Chan et al., "Emulating one-dimensional resonant Q-matching behavior in a two-dimensional system via Fano resonances," *Phys. Rev. A* **74**, 1–4 (2006).
15. I. Celanovic, N. Jovanovic, and J. Kassakian, "Two-dimensional tungsten photonic crystals as selective thermal emitters," *Appl. Phys. Lett.* **92**, 193101 (2008).
16. Y. Nam et al., "Solar thermophotovoltaic energy conversion systems with two-dimensional tantalum photonic crystal absorbers and emitters," *Sol. Energy Mater. Sol. Cells* **122**, 287–296 (2014).
17. S. John and R. Wang, "Metallic photonic-band-gap filament architectures for optimized incandescent lighting," *Phys. Rev. A.* **78**(October), 1–10 (2008).

18. J. M. Gee et al., "Selective emitters using photonic crystals for thermophotovoltaic energy conversion," in *Conf. Record of the Twenty-Ninth IEEE Photovoltaic Specialists Conf.*, pp. 896–899 (2002).
19. M. Florescu et al., "Improving solar cell efficiency using photonic band-gap materials," *Sol. Energy Mater. Sol. Cells* **91**, 1599–1610 (2007).
20. Y. X. Yeng et al., "Enabling high-temperature nanophotonics for energy applications," *Proc. Natl. Acad. Sci* **109**, 2280–2285 (2012).
21. V. Rinnerbauer et al., "Recent developments in high-temperature photonic crystals for energy conversion," *Energy Environ. Sci.* **5**, 8815 (2012).
22. V. Rinnerbauer et al., "High-temperature stability and selective thermal emission of polycrystalline tantalum photonic crystals," *Opt. Express* **21**(9), 11482–11491 (2013).
23. W. R. Chan et al., "Toward high-energy-density, high-efficiency, and moderate-temperature chip-scale thermophotovoltaics," *Proc. Natl. Acad. Sci* **110**(14), 5309–5314 (2013).
24. A. Lenert et al., "A nanophotonic solar thermophotovoltaic device," *Nat. Nanotechnol.* **9**(January), 1–5 (2014).
25. Y. Fink et al., "A dielectric omnidirectional reflector," *Science* **282**(5394), 1679–1682 (1998).
26. B. G. Bovard, "Rugate filter theory: an overview," *Appl. Opt.* **32**(3), 5427–5442 (1993).
27. R. Black, L. Martin, and P. F. Baldasaro, "Thermophotovoltaics-development status and parametric considerations for power applications," in *Eighteenth Int. Conf. on Thermoelectrics*, pp. 639–644 (1999).
28. A. Heinzel et al., "Radiation filters and emitters for the NIR based on periodically structured metal surfaces," *J. Mod. Opt.* **47**, 2399–2419 (2000).
29. U. Ortabasi and B. G. Bovard, "Rugate technology for thermophotovoltaic (TPV) applications: a new approach to near perfect filter performance," in *Fifth Conf. on Thermophotovoltaic Generation of Electricity*, Vol. 653, pp. 249–258, AIP Publishing (2003).
30. F. O'Sullivan et al., "Optical characteristics of one-dimensional Si/SiO_2 photonic crystals for thermophotovoltaic applications," *J. Appl. Phys.* **97**, 033529 (2005).
31. T. D. Rahmlow, Jr. et al., "Development of front surface, spectral control filters with greater temperature stability for thermophotovoltaic energy conversion," in *Seventh World Conf. on Thermophotovoltaic Generation of Electricity*, Vol. 890, pp. 59–67, AIP Publishing (2007).
32. B. Wernsman et al., "Greater than 20% radiant heat conversion efficiency of a thermophotovoltaic radiator/module system using reflective spectral control," *IEEE Trans. Electron Devices* **51**, 512–515 (2004).
33. P. Bermel et al., "Design and global optimization of high-efficiency thermophotovoltaic systems," in *5th World Conf. Photovoltaic Energy Conversion/Ninth Thermophotovoltaic World Conf.*, pp. 1–6 (2010).
34. A. Meulenberg and K. P. Sinha, "Spectral selectivity from resonant-coupling in microgap-TPV," 2009, http://arxiv.org/ftp/arxiv/papers/0911/0911.0860.pdf (15 February 2016).
35. M. Francoeur, R. Vaillon, and M. P. Meng, "Thermal impacts on the performance of nanoscale-gap thermophotovoltaic power generators," *IEEE Trans. Energy Convers.* **26**, 686–698 (2011).
36. Y. Guo et al., "Thermal excitation of plasmons for near-field thermophotovoltaics," *Appl. Phys. Lett.* **105**, 073903 (2014).
37. D. Peykov et al., "Effects of surface diffusion on high temperature selective emitters," *Opt. Express* **23**(8), 9979–9993 (2015).
38. A. Taflove and S. C. Hagness, *Computational Electrodynamics: The Finite-Difference Time-Domain Method*, Artech House, Norwood, Massachusetts (2000).
39. Z. Zhou, Q. Chen, and P. Bermel, "Prospects for high-performance thermophotovoltaic conversion efficiencies exceeding the Shockley–Queisser limit," *Energy Convers. Manage.* **97**, 63–69 (2015).
40. N.-P. Harder and M. A. Green, "Thermophotonics," *Semicond. Sci. Technol.* **18**(5), S270–S278 (2003).
41. J. B. Chou et al., "Enabling ideal selective solar absorption with 2D metallic dielectric photonic crystals," *Adv. Mater.* **26**(47), 8041–8045 (2014).

42. Y. X. Yeng et al., "Global optimization of omnidirectional wavelength selective emitters/absorbers based on dielectric-filled anti-reflection coated two-dimensional metallic photonic crystals," *Opt. Express* **22**, 21711 (2014).
43. Q. Chen et al., "TPV efficiency simulation," 2013, nanoHUB.org (24 September 2015).
44. A. Mathur, E. S. Sakr, and P. Bermel, "TPXSIM: a modeling tool for high efficiency thermophotovoltaic systems," 2014, docs.lib.purdue.edu/cgi/viewcontent.cgi?filename=1&article=1215&context=surf&type=additional (15 February 2016).
45. A. F. Oskooi et al., "MEEP: a flexible free-software package for electromagnetic simulations by the FDTD method," *Comput. Phys. Commun.* **181**, 687–702 (2010).
46. C. K. Carniglia, "Comparison of several shortwave pass filter designs," *Appl. Opt.* **28**, 2820–2823 (1989).
47. E. Rephaeli and S. Fan, "Absorber and emitter for solar thermo-photovoltaic systems to achieve efficiency exceeding the Shockley-Queisser limit," *Opt. Express* **17**, 15145–15159 (2009).
48. S. Roberts, "Optical properties of nickel and tungsten and their interpretation according to Drude's formula," *Phys. Rev.* **114**, 104–115 (1959).
49. E. R. G. Eckert and E. M. Sparrow, "Radiative heat exchange between surfaces with specular reflection," *Int. J. Heat Mass Transf.* **3**, 42–54 (1961).
50. F. Incropera and D. DeWitt, *Fundamentals of Heat Transfer*, John Wiley and Sons, New York (1981).

Zhiguang Zhou is a graduate research assistant at Birck Nanotechnology Center, Purdue University. He received his BS degree in physics from Fudan University, China, in 2013. He is now a direct PhD student working with Dr. Peter Bermel in the School of Electrical and Computer Engineering at Purdue. His current research interests include high-performance (solar) thermophotovoltaic systems and novel selective thermal emitters.

Omar Yehia is an undergraduate research assistant at Maurice J. Zucrow Laboratories at Purdue University. He is currently completing his Bachelor of Science in mechanical engineering from Purdue University. His current research interests include thermophotovoltaic systems, microscale combustion, and nanoscale composite energetic materials.

Peter Bermel is an assistant professor of electrical and computer engineering at Purdue University. His work improves photovoltaic, thermophotovoltaic, and nonlinear systems using the principles of nanophotonics. He has widely published in scientific peer-reviewed journals, and has been cited 3500 times. Key topics include understanding light trapping in thin-film photovoltaics; fabricating three-dimensional inverse opal photonic crystals for photovoltaics; designing high-performance thermophotovoltaic systems; and enabling photon recycling for high-efficiency lighting.